

Essay on Magnetic-Wind Mills

Part I : Analysis and Design

J.L. Duarte

Dept. Electrical Engineering (Ret.)
Eindhoven University of Technology
The Netherlands

Abstract—A methodology for the synthesis of a prime mover is presented, based only on attraction/repulsion of permanent magnets. A design example for a demonstration prototype is given, which has the potential to deploy, in theory, the sustainable generation of 22W mechanical power at 1000 rpm and beyond.

I. INTRODUCTION

There are quite a few methods for the description of magnetic forces as created by permanent magnets (PMs) [1]. However, although all the approaches converge to the same values in what concerns the *global* forces between PMs, the derived *local* forces are fundamentally different, implying that force density in each approach is rather a mathematical abstraction without necessarily a physical meaning [2]. Otherwise stated, consensus about a method for the *accurate* calculation of *torques* between PMs in close proximity is not found in the literature, and validation of results by experimental measurements are unavoidable [3], [4].

A commonly considered tool for modeling PMs consists on calculating magnetic forces among filamentary current loops. It is asserted in [6], on account of analytical equations starting from the Lorentz Force law, that a constrained displacement of an arrangement of filamentary current loops adds excess mechanical energy to the system moving parts, as long as the currents in the loops are kept *constant* during the closed translational orbit, and the *global* magnetic forces between loops are assumed to act concentrated on the loop geometric centers.

This modeling attempt based on centered global forces, instead of incremental *local* forces acting on loop segments, has led to similar results as vindicated in [7], where another calculation approach is used, namely the numerical solution of Maxwell stress tensors through FEM software. The outcomes in [7], [8] seemingly yield energy excess under constrained translational trajectories of PMs.

In order to pave the way for experimental verification of the provocative theoretical expectations above, this article presents the analysis and design of a first-principles-first prototype, idyllically denominated a *magnetic-wind mill*, being devised as the aggregation of simple prime-mover cells based on PMs. The magnets are modeled as the superposition of filamentary loops with constant current. However, the global magnetic forces are assumed to push the "center of mass" of the intrinsic magnetic dipole moments confined by the loops, and do not

act on the Amperian currents, similar to [6]. The motivation why is considered in Section VI. In the Appendix, equivalent results are illustrated when the global forces are considered to actuate on the "center of field heaviness" of the loops.

Accordingly, the intention in the following sections is to project a device wherein the elementary cells operating together create a persistent smooth torque, sufficient to deploy enough sustainable mechanical energy for conclusive measurements. The methodology developed hereinafter details the necessary analysis tools for this purpose. The design of a small mill is presented, aiming at generating about 22W when rotating at 1000 rpm. Future experiments are planned to confirm or invalidate the feasibility of these apparently hopeless theoretical statements.

II. ELEMENTARY PRIME-MOVER CELL

The concept for an initial source of motive power is shown in Fig. 1. The gearing (this case cog-wheels), assembled together with the rotors in spinning shafts, impose a constrained translation for the permanent magnets. The resulting attraction/repulsion forces among the magnets during the translational displacement lead to asymmetric torque characteristics, as shown in the sequence. A consequence of this is that, in theory, a modular structure with stacked prime-mover cells sharing the same shafts yields the sustainable generation of mechanical energy.

III. ASYMMETRIC TORQUE CHARACTERISTICS

A. Modeling of a permanent magnet

The magnetic dipole is the fundamental element of magnetism. It can be thought as a small current loop with dipole moment \vec{m} [Am²]. Statistically, one can speak about a net magnetization \vec{M} [A/m], representing the limit ratio of dipole moments per volume of magnetic material.

Contrary to the behavior of ferromagnetic materials, in a PM with homogeneous and uniform magnetization, there is barely interaction of the magnetic dipoles with an externally applied magnetic field. The magnetization is practically constant up to a high level of external coercive field, found to be [1]

$$\vec{M} = \frac{\vec{B}_r}{\mu_0}, \quad (1)$$

where \vec{B}_r [T] is the so-called remanent magnetic flux density of the material, and $\mu_0 = 4\pi \times 10^{-7}$ [H/m] the permeability of free space.

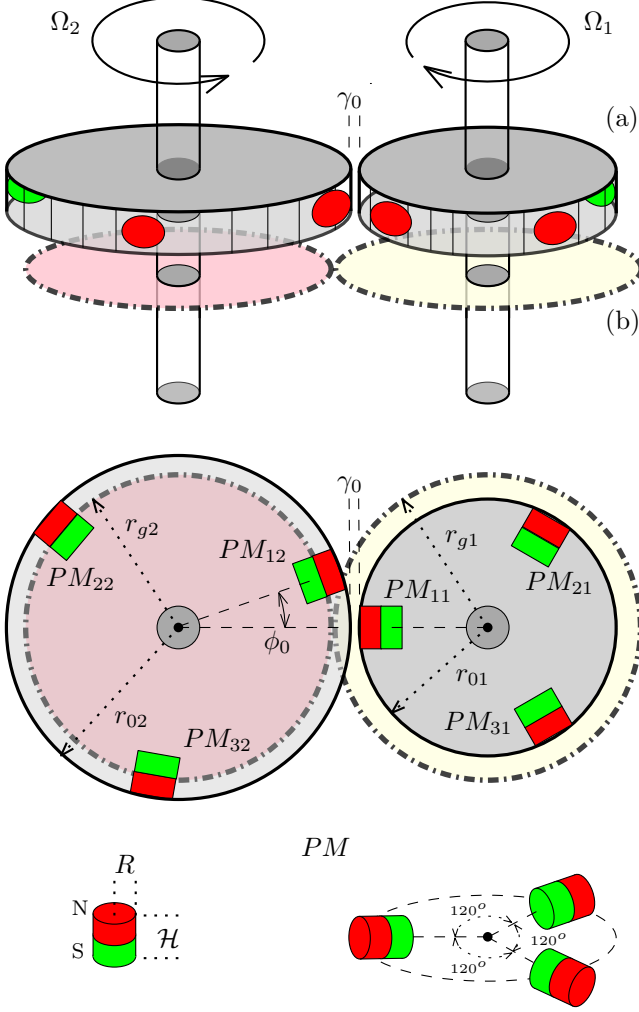


Fig. 1: Elementary prime-mover cell, consisting of (a) two rotors with embedded permanent magnets (PMs) and fixed gap separation (γ_0), and (b) a common gear mechanism, namely 1:1 cog-wheels. The angular misalignment between the rotors (ϕ_0) is kept constant by the gears in spite of rotation.

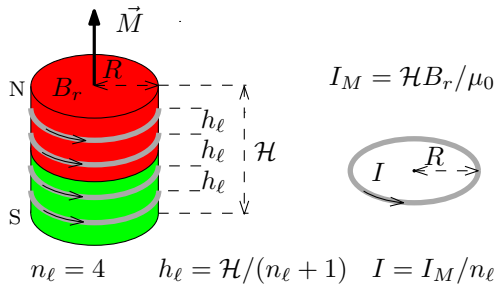


Fig. 2: Method to approximate the magnetic field created by a cylindrical PM with remanent flux density B_r as the superposition of the magnetic field engendered by n_ℓ filamentary current loops with separation h_ℓ between loops.

With regard to a PM specimen with cylindrical shape, like in Fig. 2, an analytical modeling technique is possible by assuming a fictitious magnetic surface current density on the magnet surface, given by

$$\vec{J}_M = \vec{M} \times \vec{n} [A/m], \quad (2)$$

where \vec{n} is a unity vector normal to the cylindrical surface.

So, for a magnet with height \mathcal{H} , the total equivalent magnetizing current on the surface is found to become

$$I_M = \int_{\mathcal{H}} J_M dh = \mathcal{H} B_r / \mu_0 [A]. \quad (3)$$

For expedient evaluation of magnetic forces through an analytical approach, the surface current in (3) is split and lumped in n_ℓ circular current loops with separation h_ℓ between loops, as shown in Fig. 2. The resulting force between magnets is then calculated as the superposition of the forces among all the equivalent current loops.

B. Current loops with constrained displacement

Two filamentary circular current loops with inner radii R_1 and R_2 and constant currents I_1 and I_2 , respectively, are shown in Fig. 3, centered at points C_1 and C_2 . The loop centers may translate with constant radius, r_1 and r_2 , around the pivot points P_1 and P_2 , such that C_1 , C_2 , P_1 and P_2 remain in the same plane. By given a compulsory relationship for the radial angles ϕ_1 and ϕ_2 , a constrained joint trajectory for the loops is obtained. For the purpose of analysis, convenient orthogonal vector reference frames are designated in Fig. 3.

C. Reference frames

Fig. 4 illustrates the unity vectors in Fig. 3 in a frontal perspective with regard to the translation plane, showing clearly that the unity vectors \vec{a}_{n1} and \vec{a}_{n2} are normal to the corresponding current loop planes.

For ease of analysis, orthogonal reference frames in Figs. 3 and 4 are defined as

$$\begin{aligned} \vec{a}_{xj} &= \vec{a}_{yj} \times \vec{a}_{zj}, \quad \vec{a}_{yj} = \vec{a}_{zj} \times \vec{a}_{xj}, \quad \vec{a}_{zj} = \vec{a}_{xj} \times \vec{a}_{yj}, \\ \vec{a}_{tj} &= \vec{a}_{\ell j} \times \vec{a}_{nj}, \quad \vec{a}_{\ell j} = \vec{a}_{nj} \times \vec{a}_{tj}, \quad \vec{a}_{nj} = \vec{a}_{tj} \times \vec{a}_{\ell j}, \\ \text{with } j &= \{1, 2\} \text{ and} \\ \vec{a}_{x2} &= -\vec{a}_{x1}, \quad \vec{a}_{y2} = -\vec{a}_{y1}, \quad \vec{a}_{z2} = \vec{a}_{z1}, \\ \vec{a}_{\ell 2} &= -\vec{a}_{\ell 1}, \quad \vec{a}_{\ell 1} = \vec{a}_{y2}, \end{aligned} \quad (4)$$

where ' \times ' denotes vector cross product.

On account of the sign convention for the radial angles ϕ_1 and ϕ_2 in Fig. 4, the transformations between reference frames follow from

$$\begin{aligned} \begin{bmatrix} \vec{a}_{tj} \\ \vec{a}_{nj} \end{bmatrix} &= \begin{bmatrix} -\sin \phi_j & \cos \phi_j \\ \cos \phi_j & \sin \phi_j \end{bmatrix} \begin{bmatrix} \vec{a}_{xj} \\ \vec{a}_{zj} \end{bmatrix}, \quad j = \{1, 2\}; \\ \begin{bmatrix} \vec{a}_{xj} \\ \vec{a}_{zj} \end{bmatrix} &= \begin{bmatrix} -\sin \phi_j & \cos \phi_j \\ \cos \phi_j & \sin \phi_j \end{bmatrix} \begin{bmatrix} \vec{a}_{tj} \\ \vec{a}_{nj} \end{bmatrix}, \quad j = \{1, 2\}; \\ \begin{bmatrix} \vec{a}_{ti} \\ \vec{a}_{ni} \end{bmatrix} &= \begin{bmatrix} \sin \phi_i & \cos \phi_i \\ -\cos \phi_i & \sin \phi_i \end{bmatrix} \begin{bmatrix} \vec{a}_{xj} \\ \vec{a}_{zj} \end{bmatrix}, \quad i, j = \{1, 2; 2, 1\}; \\ \begin{bmatrix} \vec{a}_{xi} \\ \vec{a}_{zi} \end{bmatrix} &= \begin{bmatrix} \sin \phi_j & -\cos \phi_j \\ \cos \phi_j & \sin \phi_j \end{bmatrix} \begin{bmatrix} \vec{a}_{tj} \\ \vec{a}_{zj} \end{bmatrix}, \quad i, j = \{1, 2; 2, 1\}; \\ \begin{bmatrix} \vec{a}_{ti} \\ \vec{a}_{ni} \end{bmatrix} &= \begin{bmatrix} \cos \phi_{ij} & \sin \phi_{ij} \\ \sin \phi_{ij} & -\cos \phi_{ij} \end{bmatrix} \begin{bmatrix} \vec{a}_{tj} \\ \vec{a}_{nj} \end{bmatrix}, \quad i, j = \{1, 2; 2, 1\}; \end{aligned} \quad (5)$$

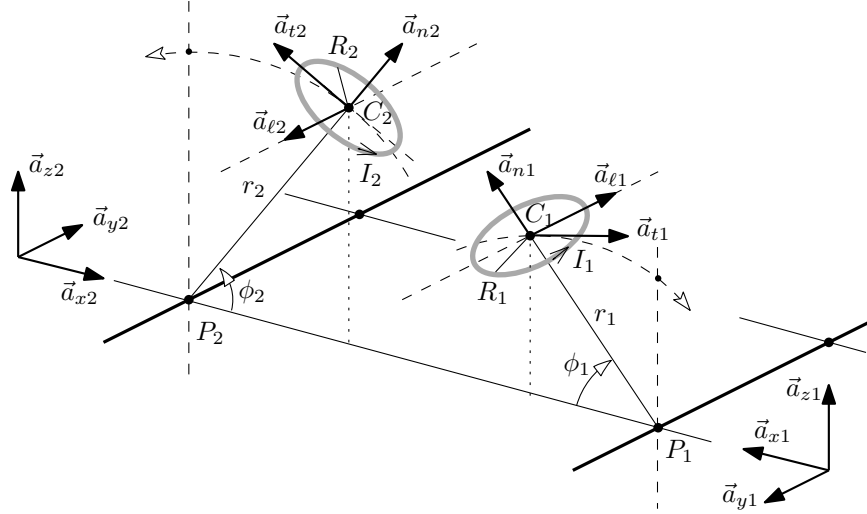


Fig. 3: Filamentary current loops with angular misalignment. The loops translate on the same plane with constant radii around fixed pivot points.

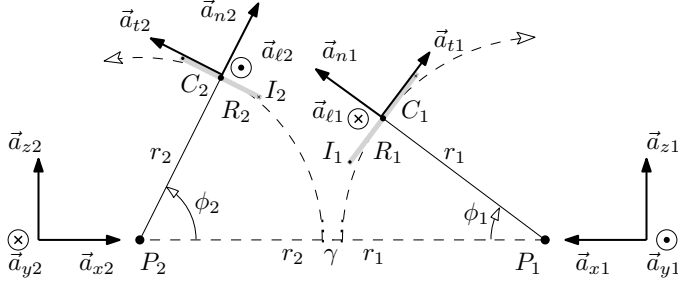


Fig. 4: Orthogonal vector reference frames from Fig. 3 shown in a frontal perspective.

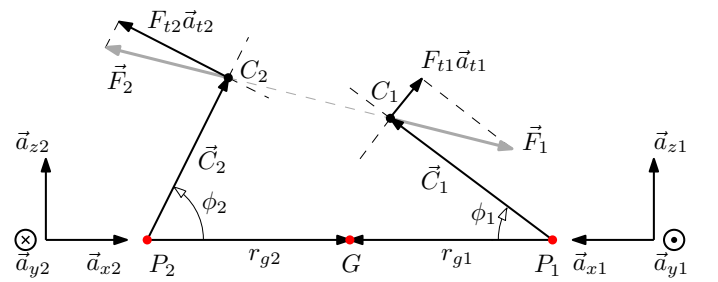


Fig. 5: Force pairs as created by magnetic repulsion/attraction between current loops constrained by cog-wheels. The forces are assumed to act on the loop geometric centers.

with

$$\phi_{12} = \phi_{21} = \phi_1 + \phi_2. \quad (6)$$

It is also assumed in Fig. 4 that the sum $r_1 + \gamma + r_2$ is constant, being equal to

$$r_1 + \gamma + r_2 = \Sigma_0 = r_{02} + \gamma_0 + r_{01}, \quad (7)$$

where $r_1 \leq r_{01}$, $r_2 \leq r_{02}$, $\gamma \geq \gamma_0$, with r_{01}, r_{02}, γ_0 defined in Fig. 1.

As an example of frame transformation, the vector linking the loop centers C_1 to C_2 ,

$$\begin{aligned} \vec{C}_{21} &= r_2 \vec{a}_{n2} + \Sigma_0 \vec{a}_{x1} - r_1 \vec{a}_{n1}, \\ \vec{C}_{21} &= \begin{bmatrix} r_2 \cos \phi_2 & r_2 \sin \phi_2 \end{bmatrix} \begin{bmatrix} \vec{a}_{x2} \\ \vec{a}_{z2} \end{bmatrix} + \begin{bmatrix} \Sigma_0 & 0 \end{bmatrix} \begin{bmatrix} \vec{a}_{x1} \\ \vec{a}_{z1} \end{bmatrix} + \\ &+ \begin{bmatrix} r_1 \cos \phi_1 & r_1 \sin \phi_1 \end{bmatrix} \begin{bmatrix} \vec{a}_{x1} \\ \vec{a}_{z1} \end{bmatrix}, \end{aligned}$$

when referenced to $(\vec{a}_{t1}, \vec{a}_{n1})$, can be found from (5) as

$$\begin{aligned} \vec{C}_{21} &= -(\Sigma_0 \sin \phi_1 - r_2 \sin \phi_{12}) \vec{a}_{t1} \\ &+ (\Sigma_0 \cos \phi_1 - r_2 \cos \phi_{12} - r_1) \vec{a}_{n1}. \end{aligned} \quad (8)$$

D. Static forces and torques

Fig. 5 illustrates a static situation, showing the magnetic forces on the current loops in Fig. 3 when a gearing such as cog-wheels is applied. The loop centers are located at

$$\vec{C}_1 = r_1 \vec{a}_{n1} \text{ and } \vec{C}_2 = r_2 \vec{a}_{n2} \quad (9)$$

relatively to the pivot points P_1 and P_2 , respectively. Point G is fixed in space and lies at the interface contact between sides of the cog-wheels in Fig. 1, the gearing having also pivot points at P_1 and P_2 and constant radii r_{g1} and r_{g2} , with gear ratio $\rho_{21} = r_{g2}/r_{g1} = 1$. Also note, with regard to Fig. 4 and (7), that $r_{g1} + r_{g2} = \Sigma_0$.

The resulting magnetic forces actuating on the current loops, \vec{F}_1 and \vec{F}_2 , form a repulsion/attraction pair, that is,

$$\vec{F}_1 + \vec{F}_2 = 0. \quad (10)$$

These *global* forces originate from the integration of magnetic forces on incremental current loop segments, and can be determined following the approach in [?] (also detailed in [6]). For ease of derivation, it is convenient to consider the total force \vec{F}_2 on loop #2, which is a consequence of current

circulation through loop #1, with reference to a vectorial frame placed on loop #1 as

$$\vec{F}_2 = \mathcal{F}_{t21} \vec{a}_{t1} + \mathcal{F}_{n21} \vec{a}_{n1}, \quad (11)$$

since $\mathcal{F}_{t21} \equiv \mathcal{F}_{t21}(\phi_1, \phi_2)$, $\mathcal{F}_{n21} \equiv \mathcal{F}_{n21}(\phi_1, \phi_2)$ may be then determined by purely analytical equations. Eventually, when necessary to consider \vec{F}_2 with reference to a frame placed on loop #2 as

$$\vec{F}_2 = F_{t2} \vec{a}_{t2} + F_{n2} \vec{a}_{n2}, \quad (12)$$

it results from (4) and (11) that

$$\begin{aligned} \vec{F}_2 &= \begin{bmatrix} \mathcal{F}_{t21} & \mathcal{F}_{n21} \end{bmatrix} \begin{bmatrix} \vec{a}_{t1} \\ \vec{a}_{n1} \end{bmatrix}, \\ \vec{F}_2 &= \begin{bmatrix} \mathcal{F}_{t21} & \mathcal{F}_{n21} \end{bmatrix} \begin{bmatrix} \cos \phi_{12} & \sin \phi_{12} \\ \sin \phi_{12} & -\cos \phi_{12} \end{bmatrix} \begin{bmatrix} \vec{a}_{t2} \\ \vec{a}_{n2} \end{bmatrix}, \end{aligned}$$

leading to

$$F_{t2} = \mathcal{F}_{t21} \cos \phi_{12} + \mathcal{F}_{n21} \sin \phi_{12}, \quad (13)$$

$$F_{n2} = \mathcal{F}_{t21} \sin \phi_{12} - \mathcal{F}_{n21} \cos \phi_{12}. \quad (14)$$

Similarly, the total force \vec{F}_1 exerted on loop #1 due to current circulation through loop #2 is referenced to a frame placed on loop #1 as

$$\vec{F}_1 = F_{t1} \vec{a}_{t1} + F_{n1} \vec{a}_{n1}. \quad (15)$$

Thereby, from (10), (11) and (15) follows

$$F_{t1} = -\mathcal{F}_{t21} \ \& \ F_{n1} = -\mathcal{F}_{n21}. \quad (16)$$

Once $\mathcal{F}_{t21}(\phi_1, \phi_2)$, $\mathcal{F}_{n21}(\phi_1, \phi_2)$ are known, under the supposition that the magnetic forces are concentrated on the geometric loop centers (more about that in Section VI), the associated torques in Fig. 5 can be readily described. For instance, the resulting torque \vec{T}_2 around the pivot point P_2 is given by

$$\vec{T}_2 = \vec{C}_2 \times \vec{F}_2 - \rho_{21} (\vec{C}_1 \times \vec{F}_1), \text{ or} \quad (17)$$

$$\vec{T}_2 = -T_2(\phi_1, \phi_2) \vec{a}_{y2}, \quad (18)$$

where $\rho_{21} = r_{g2}/r_{g1}$ is the gear ratio. The minus sign in (18) has been introduced for later display convenience, indicating that \vec{T}_2 acts in the c.c.w. direction when $T_2(\phi_1, \phi_2) > 0$. Combining (9), (11), (15) and (17), after some manipulations it is found that in (18)

$$T_2(\phi_1, \phi_2) = (r_2 \cos \phi_{12} - \rho_{21} r_1) \mathcal{F}_{t21} + (r_2 \sin \phi_{12}) \mathcal{F}_{n21} \quad (19)$$

When ϕ_1 and ϕ_2 are constrained as

$$\phi_1 = \rho_{21} \theta \ \& \ \phi_2 = \theta + \phi_0 \text{ with } \theta = \int d\theta, \quad (20)$$

it is shown in the following section that, for a special choice of parameters,

$$\langle T_2 \rangle = \frac{1}{2\pi} \int_0^{2\pi} T_2(\phi_1, \phi_2) d\theta \neq 0. \quad (21)$$

Otherwise stated, the average torque $\langle T_2 \rangle$ can be rendered asymmetric [8].

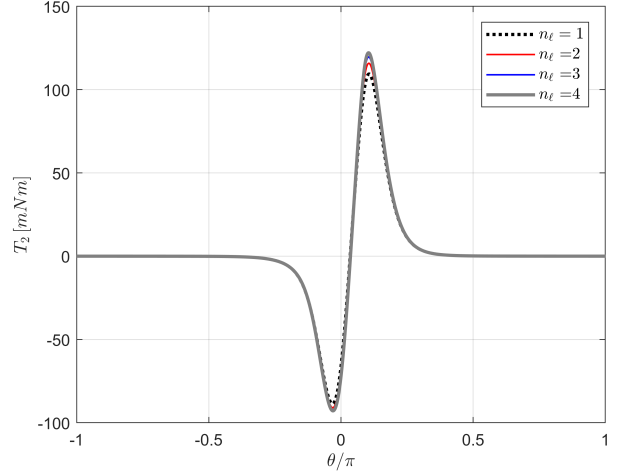


Fig. 6: Calculated static torque characteristics of a prime-mover cell with just one PM at each rotor (but keeping the radial misalignment $\phi_0 = -5^\circ$ between rotors, see Fig. 1). The magnets are modeled by sets of n_ℓ current loops and corresponding separation h_ℓ between loops (as in Fig. 2).

IV. LAYOUT OF THE MILL

Taking into account the parameters in Table I, Fig. 6 depicts the resulting asymmetric torque profile of the prime-mover cell with only one PM per rotor (instead of 3 magnets shifted by 120° as in Fig. 1). For the sake of comparison the PMs are modeled with different number of current loops n_ℓ , and salient numerical results are given in Table II.

TABLE I: Mill parameters and geometrical dimensions

Parameter	Value	Description	Fig.
r_{01} [mm]	21.0	outer radius rotor #1	(1)
r_{02} [mm]	30.0	outer radius rotor #2	
r_{g1} [mm]	26.0	outer radius gear at side #1	
r_{g2} [mm]	26.0	outer radius gear at side #2	
γ_0 [mm]	1.0	gap between rotors	
ϕ_0 [deg]	-5°	angle shift between rotors	
R [mm]	5.0	radius cylindrical PM	(2)
\mathcal{H} [mm]	3.0	height cylindrical PM	
B_r [T]	1.45	remanent flux density (NdFeB N52)	
I_M [kA]	3.5	surface Amperian current	
n_ℓ [-]	4	number of equivalent loops	
h_ℓ [mm]	0.60	separation between loops	
I [kA]	0.88	current in filamentary loop	(3)
I_1 [kA]	0.88	current in loop #1	
I_2 [kA]	0.88	current in loop #2	
R_1 [mm]	5.0	radius loop #1	
R_2 [mm]	5.0	radius loop #2	(9)
n_c [-]	8	number of stacked cells	
h_c [mm]	12.0	vertical separation between rotors	

It is possible to conclude from the outcomes in Table II that only marginal improvement in the numerical values can be expected for $n_\ell > 4$. Therefore, in the sequence it is assumed $n_\ell = 4$ in all calculations. Also note in Fig. 6 and from the results in Table II a *positive average torque systematically*

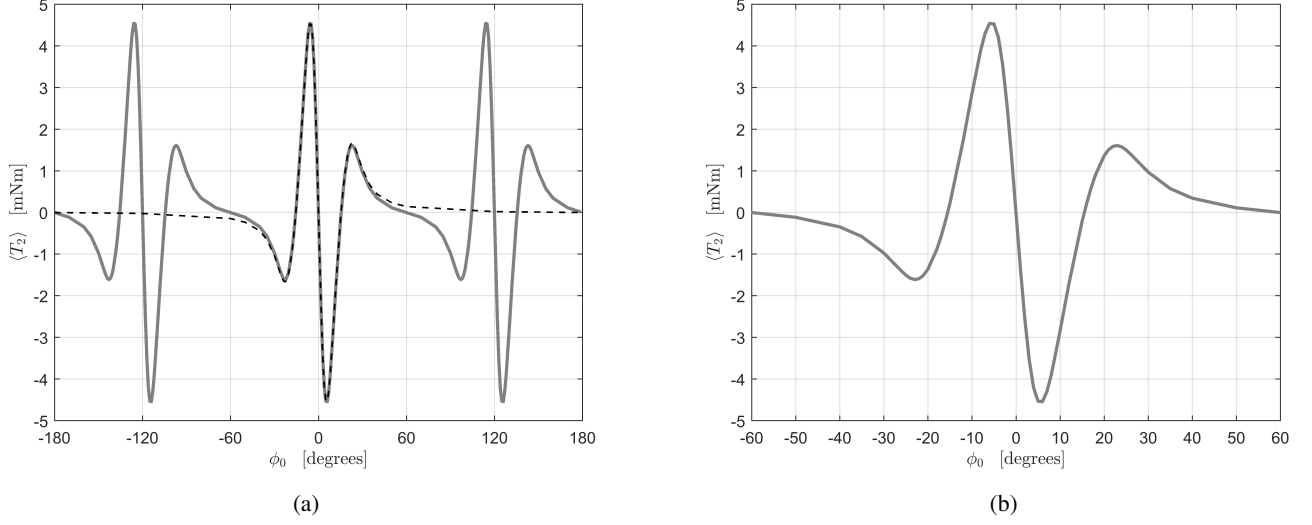


Fig. 7: (a) Calculated average torque of a prime-mover cell as function of the misalignment ϕ_0 between rotors. (b) As expected from the cell symmetry (Fig. 1), the pattern in (a) repeats at intervals of 60° . The maximum occurs for $-6^\circ \leq \phi_0 \leq -5^\circ$. The dotted trace in (a) refers to the mean torque of a simplified cell (Fig. 6 with $n_\ell = 4$).

TABLE II: Torque values in Fig. 6

n_ℓ	[-]	1	2	3	4	# equiv loops
h_ℓ	[mm]	1.50	1.00	0.75	0.60	loop separation
$\langle T_2 \rangle$	[mNm]	1.274	1.395	1.463	1.506	mean torque
T_2^{peak}	[mNm]	109.4	115.8	119.6	122.1	peak torque

arises. For instance, considering $\phi_0 = -5^\circ$, it follows from (21) that

$$\langle T_2 \rangle_0 = 1.506 \text{ mNm} \approx 1.2\% T_2^{\text{peak}}. \quad (22)$$

In Section VI this result is considered to be significant.

The choice for $\phi_0 = -5^\circ$ in Fig. 6 has been decided in view of the local maxima in Fig. 7, where the mean torque as function of ϕ_0 is shown when a complete prime-mover cell with 3 PMs per rotor is considered. The detailed torque characteristics get the repeated pattern as depicted in Fig. 8, where, again, $\phi_0 = -5^\circ$.

In Fig. 8 the average torque on the shaft becomes three times higher compared to Fig. 6, because the torque signals due to the shifted PM-pairs in Fig. 1 do not overlap. That is to say,

$$\langle T_2 \rangle_{n_c=1} = 3 \cdot \langle T_2 \rangle_0 = 4.52 \text{ mNm}. \quad (23)$$

Nevertheless, the form factor of the torque signal is still quite poor. By stacking prime-mover cells in the same shafts as show in Fig. 9, with a suitable angle shift between rotors (multiples of 45° when $n_c = 8$), a smooth average torque is the outcome (red trace in Fig. 8), with mean value given by

$$\langle T_2 \rangle_{n_c=8} = 8 \cdot \langle T_2 \rangle_{n_c=1} = 36.2 \text{ mNm} \quad (24)$$

(see also Table III). It can be shown that above a minimum required value for cell height ($h_c = 12 \text{ mm}$ for $2R = 10 \text{ mm}$), the vertical separation between stacked rotors barely impacts the torque created by the individual cells.

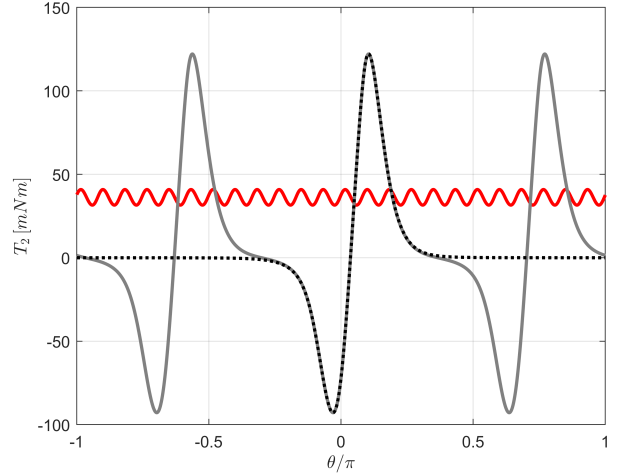


Fig. 8: Static torque profile of a prime-mover cell with 3 PM per rotor ($n_c = 1$, continued trace), and net torque profile (red trace) when stacking multiple prime-mover cells ($n_c = 8$ and $h_c = 12 \text{ mm}$) as sketched in Fig. 9. The dotted trace refers to the torque profile of a simplified cell (see Fig. 6.)

TABLE III: Torque values in Fig. 8

n_c	[-]	1	8	# cells
h_c	[mm]	-	12.0	cell separation
$\langle T_2 \rangle$	[mNm]	4.52	36.2	net mean torque
T_2^{peak}	[mNm]	122.1	40.9	peak torque

Aiming at maximizing the utilization of materials, it is opportune to interleave batteries of stacked prime-mover cells for sharing PMs, as sketched in Fig. 10, resulting a complete magnetic-wind mill. Calculations confirm that the average

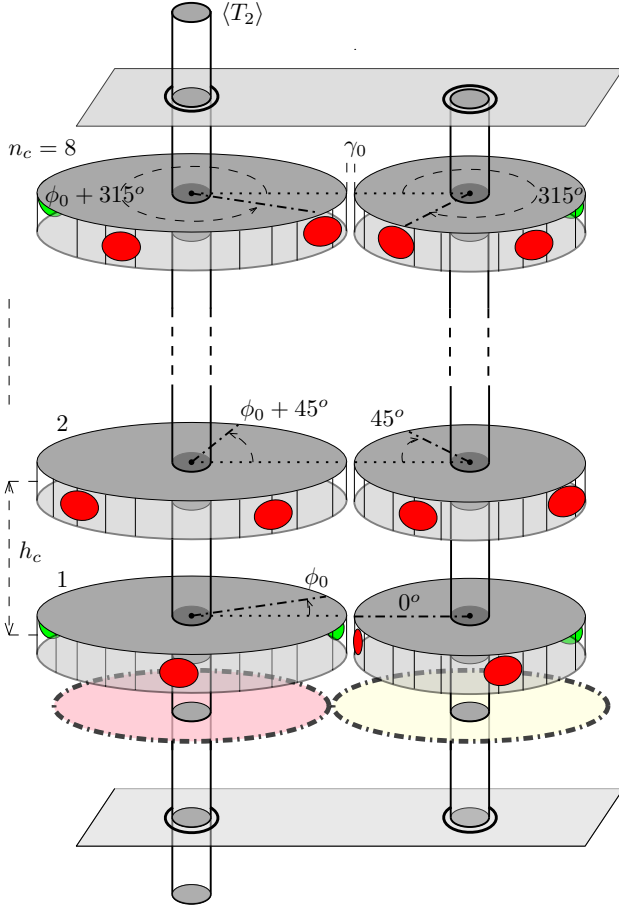


Fig. 9: Layout aiming at engineering a magnetic-wind mill that yields smooth and persistent average torque on the basis of a battery of stacked prime-mover cells.

torque created by the extra force interaction among all PMs located in the 6 cylinders at the periphery of the mill is zero. Consequently, the final average torque on the central axis in Fig. 10 is just

$$\langle T_2 \rangle_{n_c=48} = 6 \cdot \langle T_2 \rangle_{n_c=8} = 0.217 \text{ Nm}. \quad (25)$$

The resulting torque profile is depicted in Fig. 11.

Altogether, when the central cylinder of the mill is rotating with constant radial velocity Ω_2 , the average mechanical power that can be drawn from the spinning axis is found from (25) to become

$$P_2 = \Omega_2 \cdot \langle T_2 \rangle_{n_c=48}. \quad (26)$$

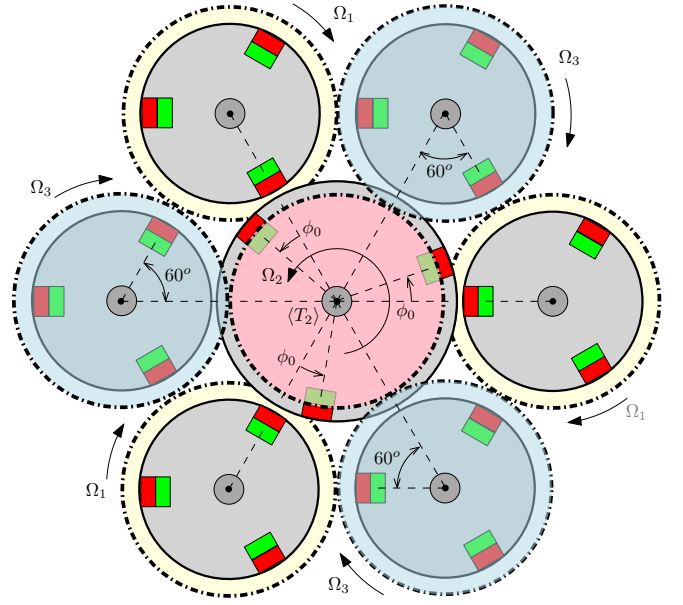
For instance,

$$\Omega_2 = 1000 \text{ rpm} \rightarrow P_2 = 22 \text{ W}. \quad (27)$$

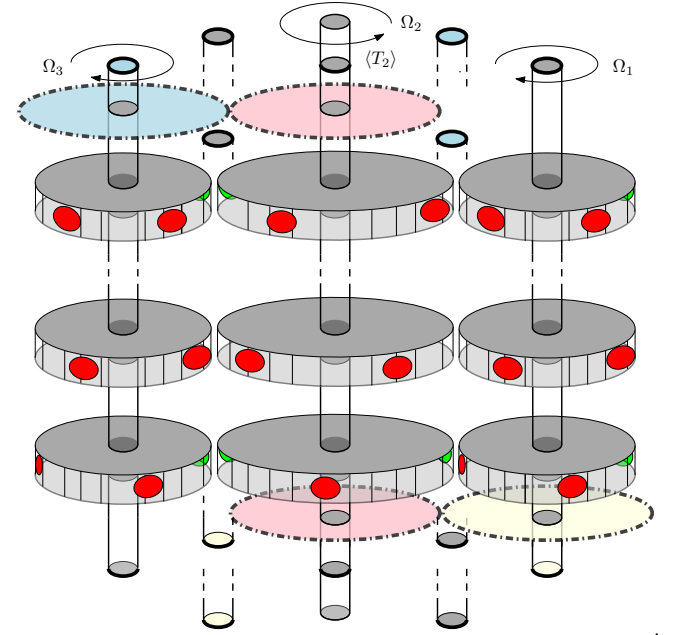
It is worthwhile to remark that P_2 in (26) increases proportionally with Ω_2 , since $\langle T_2 \rangle$ in (25) is found to be constant, being ideally independent of the rotational speed of the shaft, as justified in the next section.

V. MAGNETIC-WIND MILL IN THE FIELD

Although the results in Fig. 11 have relation to a static situation, the torque signals may be considered without change in



(a) Top view



(b) Frontal view

Fig. 10: Layout of a magnetic-wind mill with six interleaved batteries sharing stacked prime-mover cells, for the purpose of maximizing the utilization of the PMs. Note the subtle placement of the cog-wheels.

practical dynamic conditions. Since high-quality PM materials have a low relative permeability ($\mu_r \approx 1.03 - 1.05$ for sintered NdFeB) [1], the internal magnetization, \vec{M} as given in (1), is practically not affected by the proximity of another PM with similar characteristics.

Moreover, in view of the extremely low radial speeds in mechanical devices (as the one in Fig. 10) compared to the spreading velocity of EM waves in space, the dynamic regime of the net magnetic field can be considered as quasi-stationary

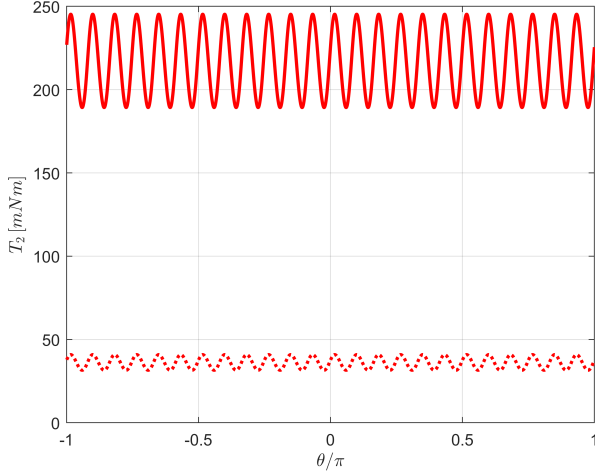


Fig. 11: Net torque characteristics of the mill sketched in Fig. 10, assembled with 6 interleaved batteries sharing prime-mover cells. The dotted trace refers to the net torque of just one battery as in Fig. 9.

(i.e. virtually instantaneous EM wave propagation).

Hence, from a modeling point-of-view, the currents through the filamentary loops may be assumed to remain constant, independent of the proximity of other loops, even under variable external magnetic flux. The only postulation is that $\mu_r = 1$ in- and outside the PMs.

Bearing in mind the construction of a laboratory prototype for experimental verification, Fig. 12 shows sketches of constituting parts for assembling a magnetic wind mill to operate in the field. It is expected that the maximum power that can be unfolded with the device will be limited by the vibrational stability of the mechanical part and by the induced eddy currents in the PM materials.

The PM magnetization, as such, is not directly impacted by electromotive forces (EMF) as induced by a time-changing magnetic flux due to the translation of neighbor PMs in the surrounding space. Nevertheless, by its turn this induced emf will produce eddy currents, therefore losses, in the PM material.

Magnet losses are usually neglected for plastic bonded or ferrite PMs, due to their quite high material resistivity. However, the resistivity of rare-earth magnetic materials (like NdFeB) is much lower, and eddy-current losses may increase the PM temperature to a point that the remanent magnetic flux density is noticeably affected, decreasing the PM performance as a consequence, as it is the case in high-speed PM motors [9].

VI. DISCUSSION

Already from the beginning of the 19th century, a well-accepted model for describing the behavior of PMs can be obtained by means of *constant* electric currents circulating on the external surface of the magnetic material, the so-called Amperian currents in (3). These imaginary superficial currents

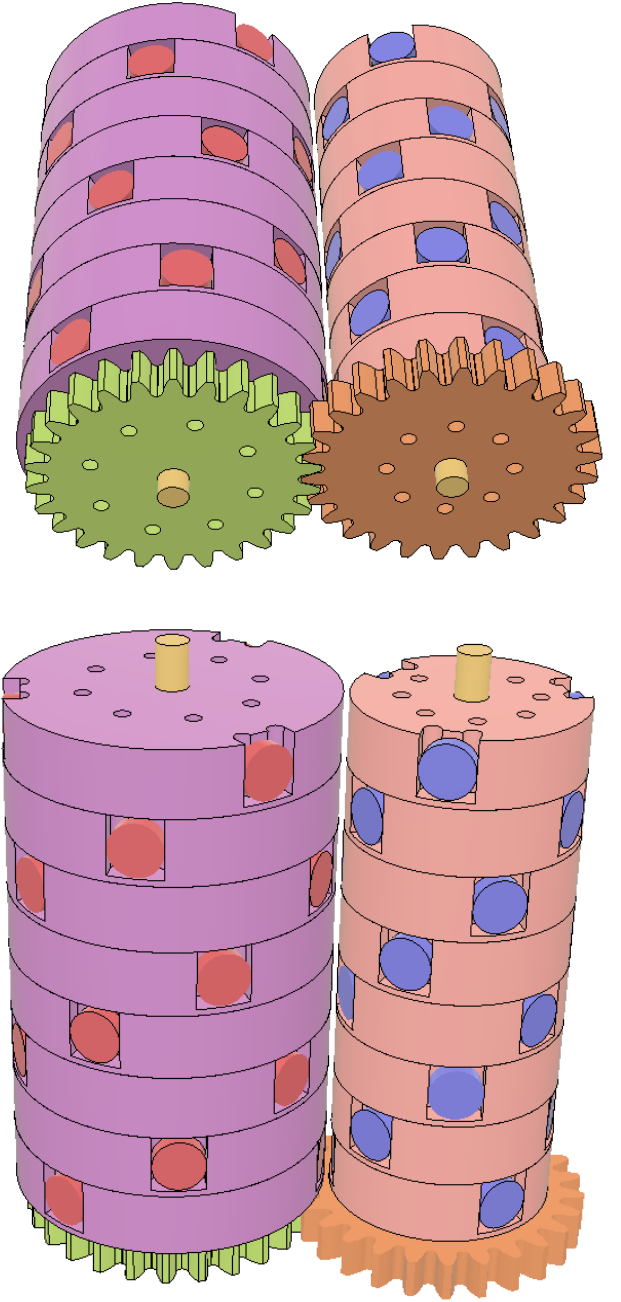


Fig. 12: Impression of mechanical parts for a mill prototype

are the macroscopic equivalent representation of the microscopic atomic activity of the internal particles of the material. In this way, the magnetic field as created by (a superposition of) filamentary current loops with constant current is generally accredited as a simple, yet quite effective, model for the *global* behavior of a PM, for which the magnetisation in (1) is constant all over the magnetic material.

Other PM modeling approaches for force derivation (equivalent magnetic charges, surface or volume integration of Maxwell stress tensors, scalar or vectorial formulation of virtual work principle) are also extensively used. In these representations, the formulas for calculation the total forces between PMs are quite accurate, irrespective the adopted

approach. However, all above methods are only globally equivalent and do not represent the actual distribution of forces in the magnetic material, leading to specific and dissimilar results for local force density on and inside the permanent magnets [2].

It is illustrative to note the discrepancies between calculated results from different methods as compared to *accurate measurements*. A systematic and significant mismatch in the calculated torque values are clearly observed [3,Figs.3-4] [4, Fig.5], in striking contrast with the ease of obtaining precise match for calculated global magnetic forces [3, Fig.5] [5, Fig.6].

Considering the two current loops in Fig. 3 as equivalent Amperian currents in PMs, it can be proven that, if the total torque on the loops is determined by the integration of magnetic forces actuating on *local* incremental loop segments, the resulting average torque per revolution is found to become zero. Though, the spacial position of the loop segments on the PM surfaces is a mathematical abstraction without physical meaning [2]. Therefore, an appealing research question would be to try developing methods to describe *total* torques based on *global* magnetic forces, since global forces can be accurately calculated and easily measured quite well [5].

In the previous sections, a try has been done by placing the global magnetic force acting on the current loop geometric center, what could be seen as concentrating the total force on the "center of mass" of the elementary magnetic dipole moments confined by the loop. Another possibility is described in the Appendix, where the global force is placed on the point that has, on average, the highest magnetic flux density, so-called the "center of field heaviness" inside the magnetic material confined by the current loop. The magnetic flux density created by current loops at arbitrary points in space are readily and precisely calculated.

Both approaches yield similar results and bring about the challenging outcome of having the average torque per revolution not equal to zero (average torque around 1% of the peak torque value). That is to say, the tentative methods herein theoretically forecast the release of usable mechanical energy.

So, the prognostic of (41) and (42) asserts that a constrained translation of PMs (modeled as a superposition of linear loops with constant current and global forces actuating not necessarily on imaginary charges) will deploy *sustainable energy* from the sources that keep the Amperian currents constant during the trajectory. As such, the source of energy that keeps going on the microscopic atomic activity in a PM, is the same source that delivers the excess energy at every revolution of the current loops, without recurrence to any further assumption.

In Sec. 4 of [6] an interpretation is given for the energy source that propels the microscopic activity of the internal particles in a PM, resorting to elementary notions from Quantum Electrodynamics. Nevertheless, aiming at an engineering project the supposition of constant Amperian currents is enough for designing and assembling prototypes.

VII. CONCLUSION

A methodology for calculating global torques between PMs in close proximity is presented, being based not on incremental

but global forces, avoiding in this way to assert a physical interpretation for imaginary currents. The model attempt leads to energy excess, allowing the portrayal of elementary prime-mover cells with PMs only. Subsequently, these cells are stacked to form batteries, and after that, batteries are interleaved to construct a mill in such a way that significant and persistent torque develops on the shaft to perform useful work. The next mandatory step to clarify the defiant theoretical outcomes will be, of course, to assemble a prototype with enough dexterity for conclusive experimental verification.

APPENDIX

Consider in Fig. 3 an arbitrary point \vec{D}_2 at the internal surface of current loop #2, with

$$\vec{D}_2 = u \vec{a}_{t2} + v \vec{a}_{\ell2}, \quad (28)$$

where $-R_2 \leq u \leq R_2$ and $-R_2 \leq v \leq R_2$.

With respect to the reference frame placed at the geometric center of loop #1, it follows from (8) that

$$\vec{D}_{21} = \vec{C}_{21} + \vec{D}_2. \quad (29)$$

After some manipulations, the components of \vec{D}_{21} are found to become

$$\vec{D}_{21} = x \vec{a}_{t1} + y \vec{a}_{\ell1} + z \vec{a}_{n1}, \text{ where} \quad (30)$$

$$x = u \cos \phi_{12} + r_2 \sin \phi_{12} - \Sigma_0 \sin \phi_1,$$

$$y = -v,$$

$$z = u \sin \phi_{12} - r_2 \cos \phi_{12} + \Sigma_0 \sin \phi_1 - r_1.$$

The magnitude of the magnetic flux density \vec{B}_{21} , as induced by current loop #1 at point \vec{D}_{21} , is calculated with

$$|\vec{B}_{21}|(u, v) = \sqrt{B_\rho^2 + B_z^2} \quad (31)$$

in which [10]

$$B_\rho = \frac{\mu_0 I_1 k z}{4\pi \rho \sqrt{R_1 \rho}} \left(-K + E \frac{R_1^2 + \rho^2 + z^2}{(R_1 - \rho)^2 + z^2} \right), \quad (32)$$

$$B_z = \frac{\mu_0 I_1 k}{4\pi \sqrt{R_1 \rho}} \left(K + E \frac{R_1^2 - \rho^2 - z^2}{(R_1 - \rho)^2 + z^2} \right), \quad (33)$$

and

$$\rho = \sqrt{x^2 + y^2}, \quad (34)$$

$$k^2 = \frac{4 R_1 \rho}{(R_1 + \rho)^2 + z^2}, \quad k = \sqrt{k^2}, \quad (35)$$

$$K = \int_0^{\pi/2} \frac{1}{\sqrt{1 - k^2 \sin^2 \xi}} d\xi,$$

$$E = \int_0^{\pi/2} \sqrt{1 - k^2 \sin^2 \xi} d\xi. \quad (36)$$

As a consequence of the intensity variations of (31) at each set of angular positions ϕ_1 and ϕ_2 , the central point ($\vec{\Gamma}_2$) of the region with the highest magnetic field magnitude, circumscribed by the surface of loop #2, has changing coordinates $u_{\Gamma2}, v_{\Gamma2}$ given by

$$\vec{\Gamma}_2 = u_{\Gamma2} \vec{a}_{t2} + v_{\Gamma2} \vec{a}_{\ell2} + r_2 \vec{a}_{n2}, \quad (37)$$

where

$$u_{\Gamma 2} = \frac{\int_{-R_2}^{R_2} \int_{-\sqrt{R_2^2-u^2}}^{\sqrt{R_2^2-u^2}} u |\vec{B}_{21}|(u, v) dv du}{\int_{-R_2}^{R_2} \int_{-\sqrt{R_2^2-u^2}}^{\sqrt{R_2^2-u^2}} |\vec{B}_{21}|(u, v) dv du} \quad (38)$$

and, due to symmetry, $v_{\Gamma 2} \equiv 0$. Similarly, it is possible to write for loop #1 that

$$\vec{\Gamma}_1 = u_{\Gamma 1} \vec{a}_{t1} + v_{\Gamma 1} \vec{a}_{\ell 1} + r_1 \vec{a}_{n1}, \quad (39)$$

Fig. 13 illustrates the variation range of $u_{\Gamma 1}$ and $u_{\Gamma 2}$ as function of the current loop rotation in Fig. 3. Circa $\pm 25\%$ displacement around the loop centers is found.

So, the vectors \vec{C}_2 and \vec{C}_1 defined in (9) could be interpreted as pointing to the "center of mass" of the current loops, while $\vec{\Gamma}_2$ in (37) and $\vec{\Gamma}_1$ in (39) point to the "center of field heaviness" of the loops, respectively. In this sense, it is to expect that, within the volume of PM material, the regions with higher magnetic field intensity are associated with higher force densities. Therefore, instead of (17) where

$$\vec{T}_2 = \vec{C}_2 \times \vec{F}_2 - \rho_{21} (\vec{C}_1 \times \vec{F}_1),$$

an alternative moment arm for calculating the resulting torque \vec{T}_2 around the pivot point P_2 is given by

$$\vec{T}_2 = \vec{\Gamma}_2 \times \vec{F}_2 - \rho_{21} (\vec{\Gamma}_1 \times \vec{F}_1). \quad (40)$$

Fig. 14 depicts the resulting asymmetric static torque profile when using (40), for which holds

$$\langle T_2 \rangle = 0.730 \text{ mNm} \text{ and } T_2^{\text{peak}} = 99.4 \text{ mNm}. \quad (41)$$

The results are quite close to the torque signal calculated with (17), also shown for comparison in Fig. 14, where

$$\langle T_2 \rangle = 1.274 \text{ mNm} \text{ and } T_2^{\text{peak}} = 109.4 \text{ mNm}. \quad (42)$$

In both cases $\langle T_2 \rangle \approx 1.0\% T_2^{\text{peak}} \neq 0$!

ACKNOWLEDGEMENTS

We would like to thank L. Kurmann, J.J. Brilman and M.A.M. Hendrix for the valuable discussions.

REFERENCES

- [1] E.P. Furlani. *Permanent magnet and Electromechanical Devices: materials, analysis and applications*. Academic Press, London, 6th ed., 2001.
- [2] L.H. de Medeiros, G. Reyne and G. Meunieros. *About the distribution of forces in permanent magnets*. IEEE Trans. on Magnetics, vol. 35, no. 3, pp. 1215-1218, 1999.
- [3] J.J. Abbott et al. *Modeling magnetic torque and force for controlled manipulation of soft-magnetic bodies*. IEEE Trans. on Robotics, vol. 23, no. 6, pp. 1247-1252, 2007.
- [4] J.L.G. Janssen et al. *Three-dimensional analytical calculation of the torque between permanent magnets in magnetic bearings*. IEEE Trans. on Magnetics, vol. 46, no. 6, pp. 1748-1751, 2010.
- [5] M.I. Gonzalez. *Forces between permanent magnets: experiments and model*. Eur. J. Phys., vol. 38, 9 pp., 2017.
- [6] J.L. Duarte. *Modeling the Yildiz Motor revisited*. Eindhoven University of Technology Research Report. July 2018. <https://doi.org/10.6100/6b67487a-bd78-4a24-bdd1-d7b9b3dbd5b7>
- [7] L. Kurmann and Y. Jia, *Oscillators with Nonpolar Magnetic Repulsion System and its Use in Rotary Nonresonant and Resonant Kinetic Energy Harvesters*, IOSR J. Applied Physics, vol. 10, no. 4, pp. 57-76, 2018.

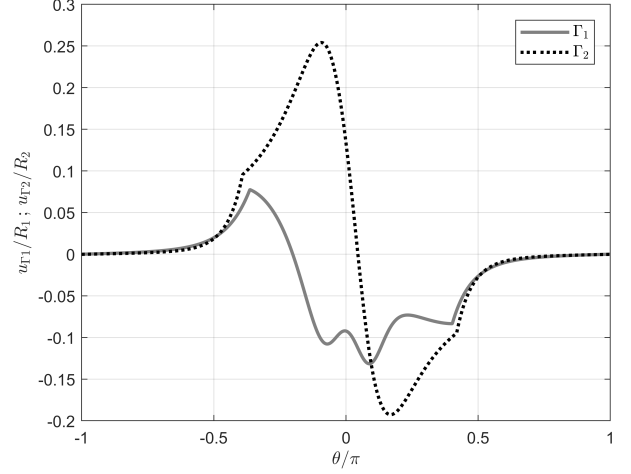


Fig. 13: Calculated displacement of $u_{\Gamma 1}$ (continuous trace) and $u_{\Gamma 2}$ (dashed trace), keeping the radial misalignment $\phi_0 = -5^\circ$ between current loops (corresponding to the situation when $n_\ell = 1$ in Fig. 6).

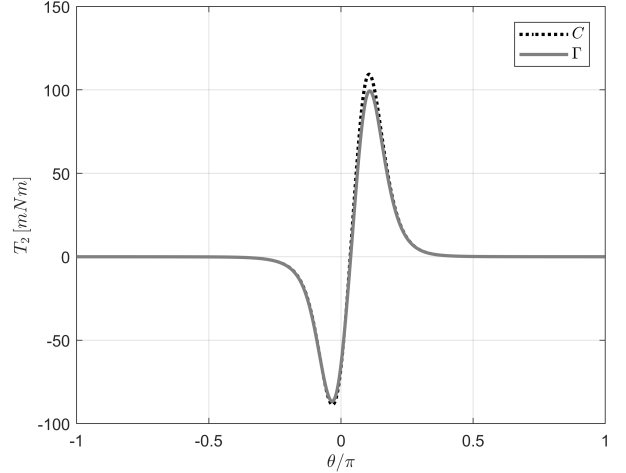


Fig. 14: Calculated static torque characteristics due to 2 current loops when taking into account the displacement of the centers of magnetic field heaviness as shown in Fig. 13 (continuous trace); and the torque signal with the magnetic forces acting on to the loop geometric centers (dashed trace, same signal as in Fig. 6 for $n_\ell = 1$).

- [8] L. Kurmann and J.L. Duarte. *Generation of asymmetric incommensurable torque signals*. Journal of Physics: Conference Series, [PW-17f]. POWERMEMS Int. Conf., Dec. 2018.
- [9] J.L.F. van der Veen, L.J.J. Offringa and A.J.A. Vandenput. *Minimising rotor losses in high-speed high-power permanent magnet synchronous generators with rectifier load*. IEE Proc., Electr.Power Appl., vol. 144, pp. 331-337, 1997.
- [10] E. Durand; *Magnétostatique*; Masson et Cie., 1968.

First appeared: February 11th, 2019

This version: November 11th, 2024

J.L. Duarte
magnetogenesis@proton.me